



Realizing efficient operations of Ni-cermet-based fuel cells on hydrocarbons via an *in situ* self-assembled metal/oxide nano-heterostructured catalyst

Kang Xu^a, Hua Zhang^a, Yangsen Xu^a, Feng Zhu^a, Fan He^a, Kotaro Sasaki^b, YongMan Choi^{c,*}, Yu Chen^{a,*}

^a School of Environment and Energy, South China University of Technology, Guangzhou 510006, China

^b Chemistry Division, Brookhaven National Laboratory, Upton, NY 11973, USA

^c College of Photonics, National Yang Ming Chiao Tung University, Tainan 71150, Taiwan

ARTICLE INFO

Keywords:

Solid oxide fuel cells
Ni-cermet anodes
Coking tolerance
Nano-heterostructure
Catalysts

ABSTRACT

Operating Ni-cermet-based fuel cells on hydrocarbons is charming but largely hindered by poor coking tolerance and severe deterioration. Here, we report an effective metal/oxide nano-heterostructured catalyst with a nominal composition of $\text{Pr}_{0.95}\text{Ru}_{0.05}\text{O}_{2-\delta}$ (PRO), which is *in situ* self-assembled to a $\text{Pr}_{0.95}\text{Ru}_{0.05-x}\text{O}_{2-\delta}$ oxide frame coated with Ru metallic nanoparticles (denoted as Ru/PRO) under the operation condition. When applied to the Ni-cermet (Ni-YSZ) anodes, the cells achieve decent peak power densities of 1.784 and 1.870 W cm⁻² on CH₄ and C₃H₈ with only 3 % H₂O at 750 °C, respectively. Moreover, the cells with Ru/PRO-coated anode demonstrate excellent durability when operated on CH₄ for ~220 h and C₃H₈ for ~115 h. It is demonstrated that the Ru/PRO generates hydroxyl species that react with carbon species, followed by the formation of COH intermediates on anode surfaces for removing the coking, as confirmed by experiments and computations.

1. Introduction

Considering the high efficiency of converting hydrocarbons to electricity, solid oxide fuel cells (SOFCs) have been regarded as one prospective energy conversion device [1–4]. However, one of the most commercial-used anodes, Ni-yttria-stabilized zirconia (Ni-YSZ) cermet, has been proven to be unsuitable for direct hydrocarbons SOFC anodes on account of the severe coking problem [5,6]. Ni shows excellent catalytic activity for the hydrogen oxidation reaction and the break of C-H bonds [7,8]. However, Ni is an extremely active catalyst for carbon deposition reactions [9]. The catalytic deactivation caused by carbon deposition inhibits the direct utilization of hydrocarbons in SOFCs. Moreover, Ni agglomeration readily occurs in the hydrocarbon atmosphere at high temperatures, likely leading to insufficient durability for long-term operations and making Ni-based cermet anodes unsuitable for direct applications in hydrocarbon-fueled SOFCs commercially [10].

For direct utilization of hydrocarbons in SOFC anodes, one strategy is to develop perovskite anodes [11–14]. For instance, Tan et al. reported a $\text{Pr}_{0.8}\text{Sr}_{1.2}\text{Ni}_{0.2}\text{Fe}_{1.3}\text{Mo}_{0.5}\text{O}_{6-\delta}$ (PSNFM) anode for directly utilizing propane [15]. During the operation, NiFe alloy nanoparticles exsolved from the dual-phase perovskites and were accompanied by the generation of

abundant oxygen vacancies, which may enhance the coking tolerance. Meanwhile, the exsolved NiFe NPs play a key role in the selective conversion of C₃H₈ to light olefins. However, regulating the chemical and thermal compatibility of the new anodes with the YSZ electrolyte is still a grand challenge [16]. Applying nano-catalysts on the anode has been confirmed to be a feasible way to increase the decomposition activity of hydrocarbons, therefore protecting the anode and enhancing the coking tolerance [17]. For instance, Yang et al. developed a novel BaO/Ni nano-interface in a commercial Ni-YSZ anode [18]. The BaO/Ni-YSZ anode cell achieved a peak power density of ~0.88 W cm⁻² at 750 °C when dry C₃H₈ was applied as the fuel. More importantly, the cell was operated on C₃H₈ for 100 h at 750 °C at a constant current density of 0.5 A cm⁻², indicating excellent carbon removal capability of the newly contrivable anode. The nano-sized BaO islands on the surface of Ni grains created abundant BaO/Ni nano-interfaces for effective water absorption. The presence of water can facilitate the carbon removal reactions in the anode. It is shown that nano-sized metal/oxide catalysts could be workable for enhancing the coking tolerance of anodes [15,18,19].

Inspired by the high activity of Ru for dissociation of H₂O/CO₂ with a (Co_{0.95}Ru_{0.05})₃O₄ bimetallic nano-structure [20], we hypothesize that a

* Corresponding authors.

E-mail addresses: ymchoi@nycu.edu.tw (Y. Choi), eschenyu@scut.edu.cn (Y. Chen).

<https://doi.org/10.1016/j.apcatb.2024.124208>

Received 15 March 2024; Received in revised form 23 April 2024; Accepted 15 May 2024

Available online 16 May 2024

0926-3373/© 2024 Elsevier B.V. All rights are reserved, including those for text and data mining, AI training, and similar technologies.

heterogeneous catalyst of Ru-doped Pr_6O_{11} could be an effective catalyst for reforming hydrocarbons and dehydrogenating propane [21–23]. In addition, it is anticipated that the Ru-doped Pr_6O_{11} anode on Ni could enhance the coke removal capability and selectively cleavage C–H bonds [3,21,24], respectively, thus leading to high performance and admirable coking tolerance. In this study, we report the rational design of the efficient nano-heterostructured catalyst for direct utilization of hydrocarbons in SOFCs, with a nominal composition of $\text{Pr}_{0.95}\text{Ru}_{0.05}\text{O}_{2.6}$ (PRO). Under the reducing environment of realistic operations, the catalyst is *in situ* restructured to a $\text{Pr}_{0.95}\text{Ru}_{0.05-x}\text{O}_{2.6}$ oxide frame coated with Ru metallic nanoparticles (denoted as Ru/PRO). When applied in the Ni-YSZ-based SOFC, cells with the Ru/PRO-coated anode demonstrated good performance, achieving peak power densities of 1.784 and 1.870 W cm^{-2} at 750 °C when operated on 3 % H_2O humidified CH_4 and C_3H_8 , respectively, while maintaining excellent coking tolerance (no obvious coking after ~220 h operation on methane or ~115 h operation

on propane).

2. Experimental

2.1. Preparation of $\text{Pr}_{0.95}\text{Ru}_{0.05}\text{O}_2$ (PRO), Pr_6O_{11} , and RuO_2 powders for characterization

$\text{Pr}_{0.95}\text{Ru}_{0.05}\text{O}_2$ (PRO) powder was fabricated by a citric nitrate solution combustion method. A stoichiometric amount of high-purity Pr (NO_3)₃·6 H_2O and $\text{Ru}(\text{NO})(\text{NO}_3)_x(\text{OH})_y$ were dissolved into deionized water with continuous heating and stirring. When the solid materials were dissolved, EDTA, citric acid, and ammonia were added to the mixture. The mixed solution was further heated at 90 °C with a stirring speed of 300 rpm until the solution was gelatinous. After the liquid was dried, the gel was moved to the oven and fired initially at 300 °C for 5 h. Then, the ash was calcined at 800 °C for 1 h to form PRO powder. For a

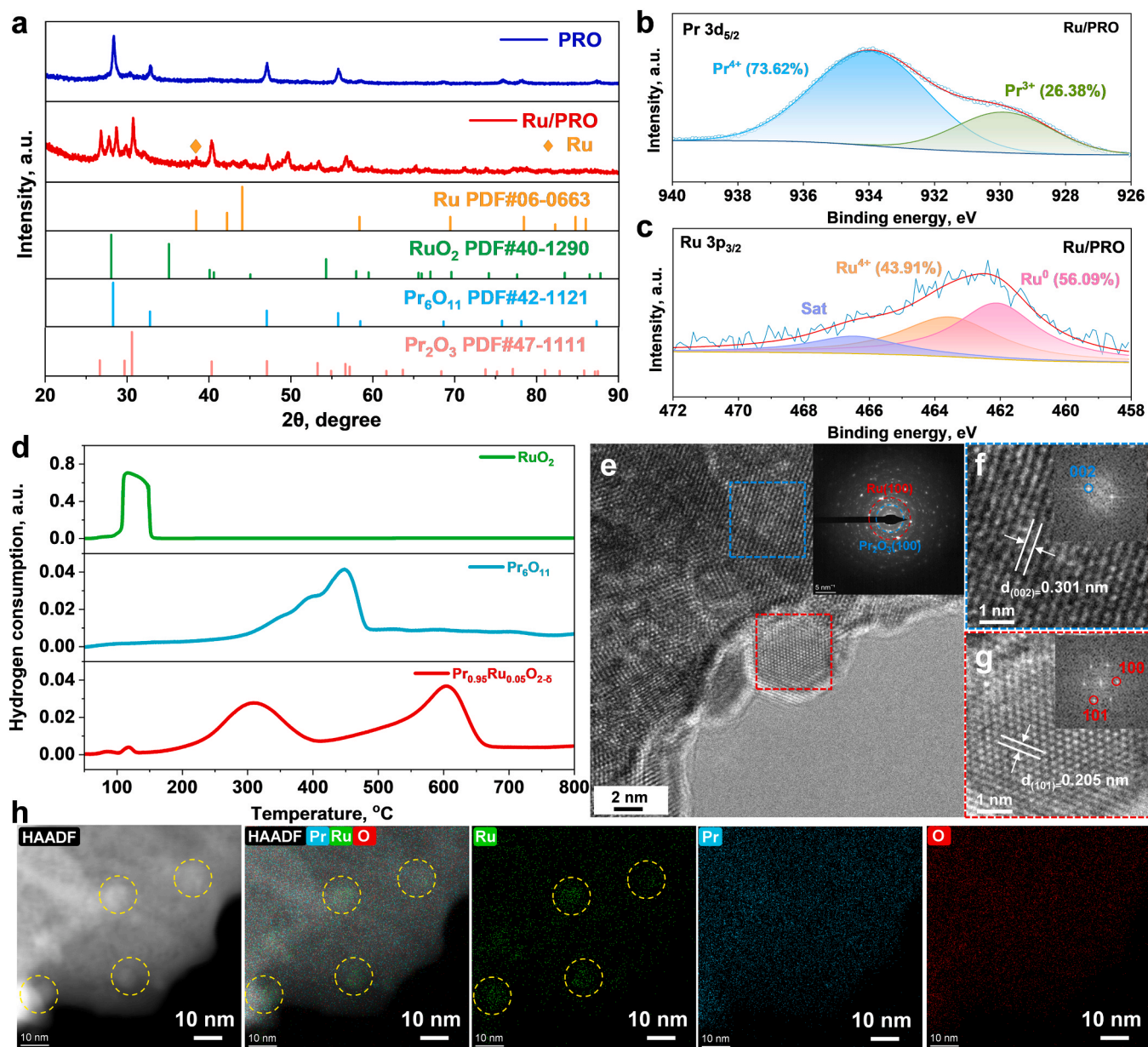


Fig. 1. Microstructure analyses of PRO catalyst. (a) XRD patterns of PRO and Ru/PRO; XPS spectra analyses of (b) Pr 3d_{5/2} and (c) Ru 3p_{3/2} of Ru/PRO; (d) H₂-TPR of RuO₂, Pr₆O₁₁, and PRO; (e) A HRTEM image of a Ru/PRO grains; the inset is a SAED image of Ru/PRO grain; (f) A HRTEM image of Pr₂O₃ substrate, the inset is the corresponding fast Fourier transform (FFT) pattern of the area in the blue box; (g) A HRTEM image of metallic Ru nanoparticle, the inset is the corresponding fast Fourier transform (FFT) pattern image of the area in the red box; (h) HAADF and corresponding EDS mapping images of Ru/PRO.

better comparison, Pr_6O_{11} , and RuO_2 powders were fabricated in the same way as the PRO sample. The reduced $\text{Ru}/\text{Pr}_{0.95}\text{Ru}_{0.05}\text{O}_2$ (Ru/PRO), Pr_6O_{11} , and RuO_2 powders were obtained by reducing $\text{Pr}_{0.95}\text{Ru}_{0.05}\text{O}_2$ (PRO), Pr_6O_{11} , and RuO_2 powders at 800 °C with 3 % H_2O humidified hydrogen for 1 h.

2.2. Preparation of $\text{Pr}_{0.95}\text{Ru}_{0.05}\text{O}_2$ catalyst for infiltration

A stoichiometric amount of high-purity $\text{Pr}(\text{NO}_3)_3 \cdot 6\text{H}_2\text{O}$ and $\text{Ru}(\text{NO}_3)_x(\text{OH})_y$ were dissolved into deionized water to form 0.1 M $\text{Pr}_{0.95}\text{Ru}_{0.05}\text{O}_2$ (PRO) catalyst solution. Then, the solution was left for 24 h to ensure all solid materials were dissolved entirely. 150 μL of PRO solution was deposited on the porous anode of an anode-supported single cell (with a load amount of $\sim 2.51\text{ mg cm}^{-2}$) via a micro-liter syringe. It is worth mentioning that 10 μL of PRO solution was infiltrated into the anode and followed by a drying process (70 °C, 0.5 h) to ensure all catalysts were deposited into the porous anode. The infiltration and drying process was repeated several times to achieve the desired catalyst loading. After being infiltrated into the anode, the catalyst was calcinated at 800 °C for 1 h to form PRO. The fabrication and infiltration method of Pr_6O_{11} , and RuO_2 catalysts are the same as PRO.

3. Results and discussion

3.1. Structure of the catalyst before and after reduction

Shown in Fig. 1a are the X-ray diffraction (XRD) patterns of as-prepared PRO and Ru/PRO , respectively. The PRO sample exhibits distinguished Pr_6O_{11} peaks (PDF#42–1121), and no apparent RuO_2 phase is detected, indicating that Ru is likely doped into the Pr_6O_{11} lattice. However, after being reduced at 800 °C with 3 % H_2O humidified hydrogen for 1 h, distinct Pr_2O_3 peaks (PDF#47–1111) appear in the XRD pattern, implying that the chemical state of Pr is changed during the reduction process (Figure S1a, Supplementary Note 1). Moreover, the distinctive metallic Ru peaks are detected in Ru/PRO , suggesting that Ru is partially reduced from the bulk phase and metallic Ru is formed (Figure S1b, Supplementary Note 1). Furthermore, X-ray photoelectron spectroscopy (XPS) was conducted to evaluate the surface electronic states of PRO and Ru/PRO . As shown in Fig. 1b, Pr in Ru/PRO exhibits two chemical states of Pr^{3+} and Pr^{4+} with 26.38 % and 73.62 %, respectively. However, the proportions of Pr^{3+} and Pr^{4+} in PRO are 25.23 % and 74.77 %, respectively (Figure S2a, Supplementary Note 2). The decrease of Pr^{4+} in Ru/PRO is consistent with the appearance of the Pr_2O_3 phase in XRD. XPS result of Ru 3p_{3/2} of the Ru/PRO powder is displayed in Fig. 1c, as shown, two mainly chemical states of Ru in the sample are Ru^{4+} and Ru^0 with an approximate percentage of 43.91 %, and 56.09 %, respectively. In contrast, Ru in PRO only demonstrates one chemical state Ru^{4+} (Figure S2b, Supplementary Note 2). The simultaneous occurrence of Ru^{4+} and Ru^0 in Ru/PRO further illustrates the partial reduction of Ru in PRO to metallic Ru. The XPS of O 1 s spectra of PRO and Ru/PRO are displayed in Figure S3 (Supplementary Note 3). In the Ru/PRO sample, the concentration of chemisorbed H_2O (O_w) demonstrates a slight increase (from 28.06 % to 31.58 %), implying the improved water uptake capability of Ru/PRO [25]. When applied to SOFCs operated on hydrocarbons, the water captured in the anode could participate in the carbon removal reactions, thus improving the coking tolerance of the anode. An H_2 -temperature programmed reduction (H_2 -TPR) is performed to study the exsolution of the catalysts during the reduction process. The profiles exhibited in Fig. 1d imply the nature of Pr and/or Ru in the catalysts. The H_2 -TPR profile of RuO_2 shows an extremely sharp peak at ~ 115 °C, which could be attributed to the property of being reduced at a relatively low temperature. The H_2 -TPR profile of Pr_6O_{11} mainly exhibits two peaks at ~ 400 °C and ~ 450 °C, corresponding to the reduction of surface partial bulk Pr^{4+} to Pr^{3+} [26,27]. For the PRO sample, a small peak appears at

~ 117 °C, attributed to the *in situ* exsolution of Ru [25], which is consistent with the XRD and XPS analyses. The peak at ~ 305 °C is likely attributed to the removal of adsorbed oxygen species and the reduction of Pr^{4+} to Pr^{3+} on the entire surface and in partial bulk. Whereas the peak at ~ 605 °C may correspond to the reduction of partial residual bulk Pr^{4+} to Pr^{3+} . [26] The reduction temperature and H_2 consumption of Pr_6O_{11} and PRO show substantial differences, indicating that the dopant of Ru may change the reduction characteristic of Pr_6O_{11} , and the reducibility of PRO is significantly enhanced.

Fig. 1e displays a high-resolution transmission electron microscopy (HRTEM) image of Ru/PRO grains; distinct nanoparticles can be observed on the substrate. The marked diffraction rings from the selected area electron diffraction (SAED) were close to (100) of metallic Ru and (100) of Pr_2O_3 , respectively. The detailed HRTEM image of the substrate (blue box in Fig. 1d) is shown in Fig. 1f; the lattice spacing of 0.301 nm corresponds to the (002) plane of Pr_2O_3 . Fig. 1g exhibits the enlarged image of a nanoparticle in Fig. 1e (red box). The lattice spacing of 0.205 nm is precisely consistent with the (101) plane of metallic Ru, indicating that the nanoparticles in Ru/PRO are likely to be metallic Ru, which is consistent with the XRD and XPS results. Shown in Figure S4 is the image of Ru/PRO grains. A large number of Ru nanoparticles appear on the substrate after being reduced (Supplementary Note 4). Fig. 1h is the images of high-angle annular dark-field (HAADF) and corresponding EDS mapping of Ru/PRO , mainly implying a local segregation of Ru element and a uniform distribution of Pr and O elements, further confirming the generation of nano-sized metallic Ru. The corresponding element concentration of the EDS mapping (with the proportion of 29.62 %, 1.57 %, and 68.81 % for Pr, Ru, and O, respectively) is displayed in Figure S5 (Supplementary Note 4), which is consistent with the stoichiometric ratio of Ru/PRO . Therefore, it is safe to conclude that a partial exsolution of the Ru element occurred on the surface of $\text{Pr}_{0.95}\text{Ru}_{0.05}\text{O}_{2-\delta}$, forming metallic nanoparticles after the reduction, as confirmed by the XRD, XPS, and TEM analyses.

3.2. Electrochemical performance of anodes in H_2

The electrochemical impedance spectra (EIS) of symmetrical cells with bare anode, RuO_2 -, Pr_6O_{11} -, and Ru/PRO -coated anodes were measured in 3 % H_2O humidified hydrogen at 650–800 °C. As displayed in Fig. 2a, the bare anode demonstrated the area-specific resistances (ASRs) of 2.25, 4.82, 10.11, and 24.09 $\Omega\text{ cm}^2$ at 800, 750, 700, and 650 °C, respectively. The Ru/PRO -coated anode demonstrated much smaller ASRs with the values of 0.79, 1.30, 2.18, and 3.90 $\Omega\text{ cm}^2$ at 800–650 °C (Fig. 2b), respectively. Fig. 2c displays the comparison of ASRs of symmetrical cells with bare, RuO_2 -, Pr_6O_{11} -, and Ru/PRO -coated anodes. The detailed EIS is displayed in Figure S6 (Supplementary Note 5). The ASRs of catalysts-coated cells demonstrate a noticeable decrease compared to the bare cell. Especially, the symmetrical cell with the Ru/PRO -coated anode exhibits the smallest ASRs at all temperatures. For example, at 700 °C, the ASRs of the Ru/PRO -coated cell show a 73 % decrease compared to the bare cell. A distribution of relaxation time (DRT) analysis was performed to understand the hydrogen oxidation process occurring in the anode. As shown in Figure S7 (Supplementary Note 6), the most significant difference appears in the intermediate frequency (IF) peak. All three catalysts-coated anodes show far smaller IF peaks than the bare anode, likely indicating that the addition of catalysts (Ru/PRO , Pr_6O_{11} , and RuO_2) in the anode can significantly accelerate the oxygen vacancy transport and/or the hydrogen oxidation reaction [28–30].

Displayed in Fig. 2d is a cross-sectional SEM image of a Ru/PRO -modified single cell after being tested on hydrogen (Figure S8, Supplementary Note 7). As shown, a multi-layered structure includes a Ni-YSZ anode support layer (ASL, $\sim 600\text{ }\mu\text{m}$), a porous Ni-YSZ anode function layer ($\sim 10\text{ }\mu\text{m}$), a dense YSZ electrolyte layer ($\sim 8\text{ }\mu\text{m}$), a porous GDC buffer layer ($\sim 3\text{ }\mu\text{m}$) and a porous PBCC cathode layer ($\sim 15\text{ }\mu\text{m}$). The electrochemical performance of the cells with the Ru/PRO -coated anode

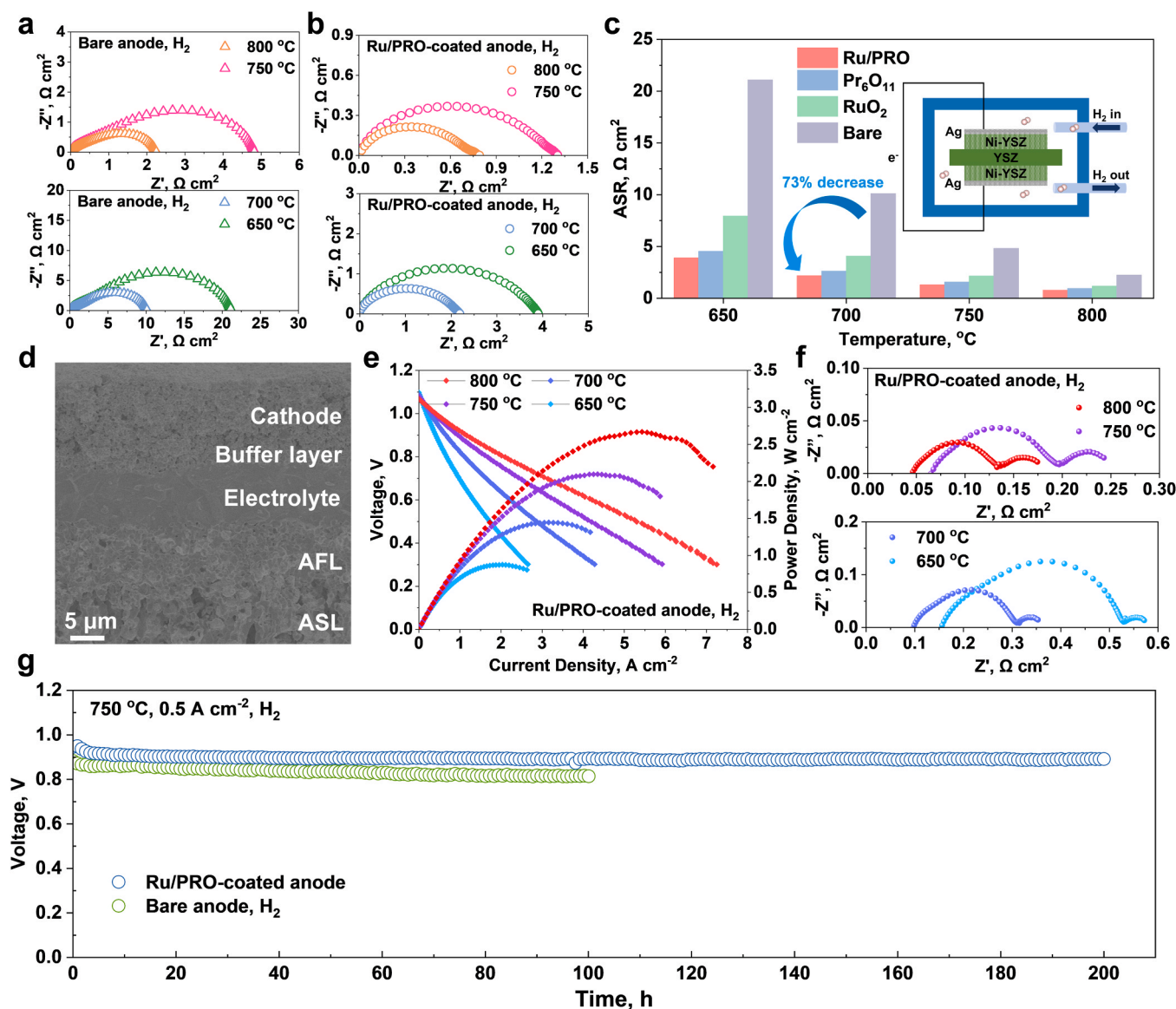


Fig. 2. Performance of anodes in H₂. (a) Typical EIS of a bare symmetrical cell; (b) Typical EIS of a Ru/PRO-modified symmetrical cell; (c) Comparison of ASRs of symmetrical cells with catalysts-coated and bare anodes at 650–800 °C in 3 % H₂O humidified hydrogen; (d) A cross-sectional SEM image of a Ru/PRO-modified single cell; (e) Typical I-V-P curves of a Ru/PRO-modified single cell; (f) Typical EIS of a Ru/PRO-modified single cell; and (g) The short-term durability evaluation of bare and Ru/PRO-modified cells.

is evaluated at 650–800 °C with 3 % H₂O humidified hydrogen as the fuel and ambient air as the oxidant. As exhibited in Fig. 2e, a single cell with the Ru/PRO-coated anode demonstrates high peak power densities (PPDs) of 2.673, 2.104, 1.449, and 0.874 W cm⁻² at 800, 750, 700, and 650 °C, respectively, with the corresponding polarization resistances (R_p s) of 0.128, 0.175, 0.254, and 0.415 Ω cm² (Fig. 2f). Higher PPDs and lower R_p s are found in Ru/PRO-coated cells, most likely due to the accelerated hydrogen oxidation process of the Ru/PRO-coated anode (Figure S9, Supplementary Note 8). Compared with the advanced oxygen ionic electrolyte-based SOFCs, our Ru/PRO-modified single cells demonstrate decent PPDs at all testing temperatures (Figure S10, Supplementary Note 9) [31–48]. Fig. 2g displays the short-term durability of bare and Ru/PRO-modified single cells in hydrogen at a constant current density of 0.5 A cm⁻² at 750 °C. The cell with the bare anode demonstrates a decay rate of 0.068 V (100 h)⁻¹, which is far faster than that in the cell with the Ru/PRO-coated anode (0.0275 V (100 h)⁻¹), supporting that coating the anode with Ru/PRO is conducive to the durability of cells.

3.3. Electrochemical performance and coking tolerance analyses on methane

Shown in Fig. 3a are the typical I-V-P curves of single cells with bare and Ru/PRO-coated anodes at 750 °C with 3 % H₂O humidified CH₄ as the fuel. A high PPD of 1.784 W cm⁻² was obtained in a Ru/PRO-modified cell, much higher than that in a bare cell (1.442 W cm⁻²). The corresponding EIS is displayed in Figure S11 (Supplementary Note 10). Shown in Fig. 3b is the comparison of the PPDs of our cells with the state-of-the-art oxygen ion conductor SOFCs reported in recent years operating on CH₄ at 750 °C [10,17,49–54]. Our cells with Ru/PRO-coated anode demonstrate high performance. Fig. 3c exhibits the short-term durability of bare and Ru/PRO-modified cells when fueled by 3 % H₂O humidified CH₄ at a constant current density of 0.75 A cm⁻² at 750 °C. After only ~10 h of operation, the voltage of the cell with the bare anode dropped to zero. In contrast, the cell with Ru/PRO-coated anode is stably operated for over 220 h (Figure S12, Supplementary Note 11). Shown in Fig. 3d is a micro-scale image of the

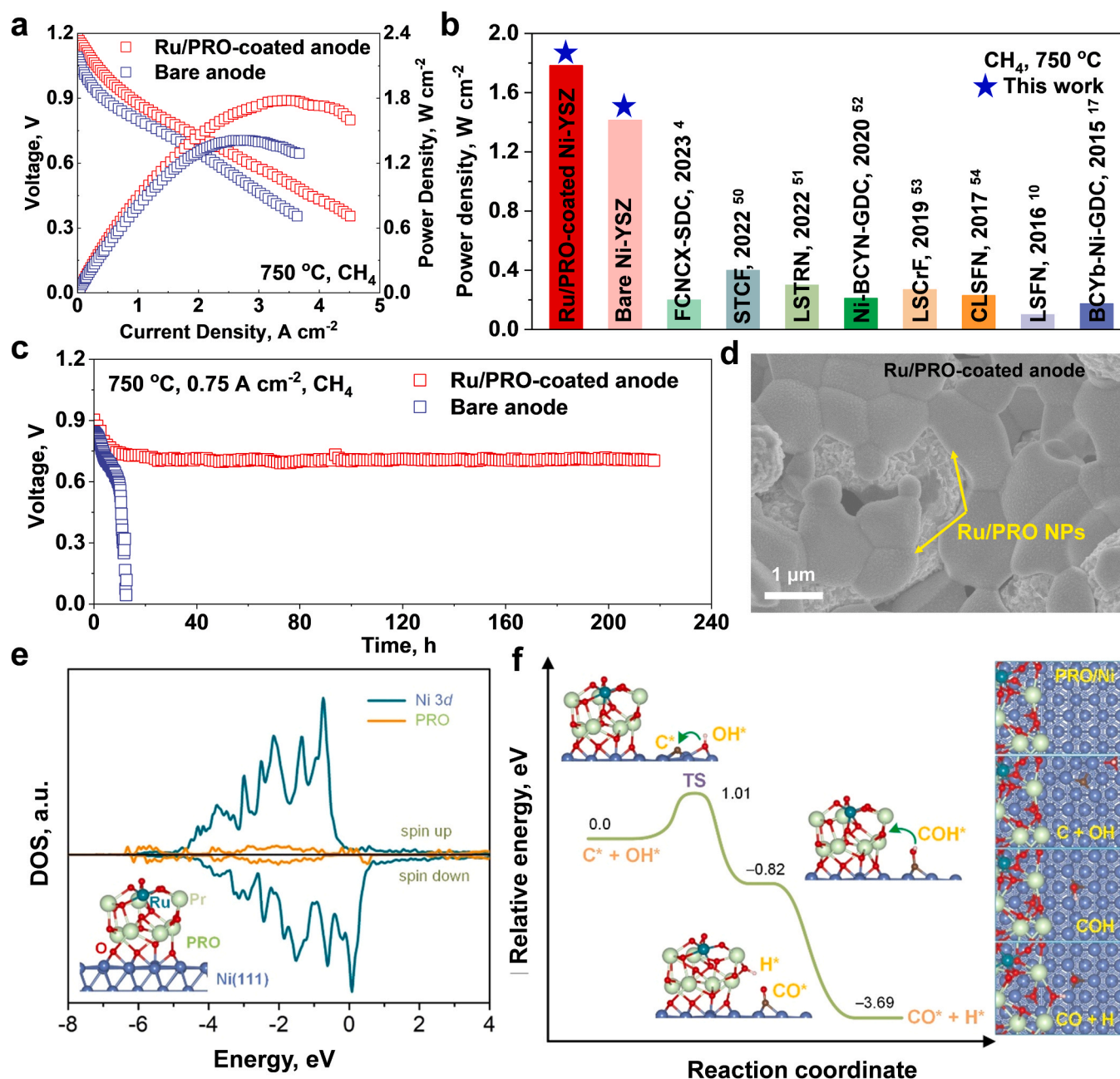


Fig. 3. Electrochemical performance and coke removal mechanism analyses on methane. (a) Typical I - V - P curves of single cells with bare and Ru/PRO-coated anodes at 750 °C with 3 % H_2O humidified CH_4 as the fuel and ambient air as the oxidant; (b) Comparison of the peak power densities of the advanced oxygen ion conductor SOFCs with CH_4 as the fuel reported in recent years; (c) Short-term durability of bare and Ru/PRO-modified cells when fueled by 3 % H_2O humidified CH_4 at a constant current density of 0.75 A cm^{-2} at 750 °C; (d) A detailed SEM image of the Ru/PRO-coated anode after the durability evaluation on CH_4 ; (e) DOS plots for PRO/Ni(111). The Fermi energy is at $E_f = 0$ eV; and (f) A proposed reaction mechanism for the coking tolerance of PRO/Ni(111) involved by a COH intermediate species. TS denotes a transition state.

Ru/PRO-coated anode after the operation of ~ 220 h on methane. No obvious coke is observed, implying the excellent coking tolerance and carbon removal capability of the Ru/PRO-coated. Figure S13 (Supplementary Note 12) displays the gas products of a CH_4 -fueled SOFC reactor at 750 °C and a current density of 0.75 A cm^{-2} . A large amount of methane is detected in the gas products. Nevertheless, after employing the Ru/PRO catalyst in the anode, the H_2 percentage significantly increases, enabling the stable operation of cells on methane.

Density functional theory (DFT) calculations were conducted to attain a mechanistic understanding of the substantially enhanced tolerance against coking of Ru/PRO using CH_4 as a fuel. As shown in Figure S14, we constructed a Ru-doped PrO_2 on the Ni(111) model

(PRO/Ni(111)) containing a small PRO chain (1 Ru, 7 Pr, and 16 O atoms) over a three-layer $p(3 \times 6)$ Ni substrate to propose a plausible reaction mechanism by connecting reactants and products through a minimum energy pathway, similar to the previous study [18,24]. As recently reported [18,24,55], we assumed that the carbon species formed from CH_4 oxidation may occur preferentially on Ni anode surfaces [18,56] under SOFC conditions, and the surface reaction of C and OH generates COH species. It is noted that OH species can be formed effectively through the surface reaction of O and H originating from oxygen ions (O^{2-}) and hydrogen species (Table S1). Accordingly, we explored the coking-tolerant mechanism near the PRO-like chains on Ni (111) to examine the carbon removal process. As displayed in Fig. 3e, we

performed the electronic structure analysis with the density of states (DOS) of the PRO/Ni(1 1 1) model, demonstrating PRO is effectively hybridized with the Ni 3d orbital. Then, as schematically shown in Fig. 3f, the most plausible reaction pathway is proposed. Firstly, carbon and hydroxyl species are preferentially formed on Ni(111) and near the interface of PRO/Ni(111), as compiled in Tables S1 and S2. Then, the C-O bond can be formed to generate a COH intermediate species by overcoming a transition state at TS with a reaction barrier of 1.01 eV, releasing energy of -0.82 eV. The vertically adsorbed COH species linked via the H-O bond with the nanostructured PRO leads to a barrierless O-H bond cleavage. It results in CO adsorbed Ni(111) and hydroxylated PRO. On the other hand, as compared in Tables S2 and Fig. 3f, the reaction barriers of COH formation and dissociation to $\text{CO} + \text{H}$ on Ni(111) are higher than those on PRO/Ni(111). Finally, as detected experimentally (Figure S13, Supplementary Note 12), electrochemical oxidation of CO and H may occur after surface diffusion to triple-phase boundaries (TPBs) ($\text{CO} + \text{O}^{2-} \rightarrow \text{CO}_2 + 2\text{e}^-$ and $\text{H}_2 + \text{O}^{2-} \rightarrow \text{H}_2\text{O} + 2\text{e}^-$) and direct CO desorption. We demonstrated that the Ru/PRO

configuration could efficiently generate hydroxyl species reacting with carbon species, followed by the formation of COH intermediates on Ni anode surfaces, boosting coking tolerance.

3.4. Co-generation of electricity and olefins on propane

In typical fuel cell testing, 3 % humidified hydrocarbons were directly fed into the porous anode. The gaseous hydrocarbons were subsequently decomposed to hydrogen, carbon monoxide, and other light hydrocarbons within the anode. As schematically shown in Fig. 4a, the cell displays a multilayer structure, including a layer of porous $\text{PrBa}_{0.8}\text{Ca}_{0.2}\text{Co}_2\text{O}_{5+\delta}$ (PBCC) cathode, a GDC buffer layer, a dense YSZ electrode, a porous Ni-YSZ anode functional layer (AFL), a Ru/PRO-coated porous Ni-YSZ anode supporting layer (ASL) with finger-like pores. The C_3H_8 conversion and coke elimination mechanism are also schematically displayed. The steam in humidified hydrocarbons and steam generated in the hydrogen oxidation reaction favor the carbon removal process. The O^{2-} transferred from the cathode and H_2O in the

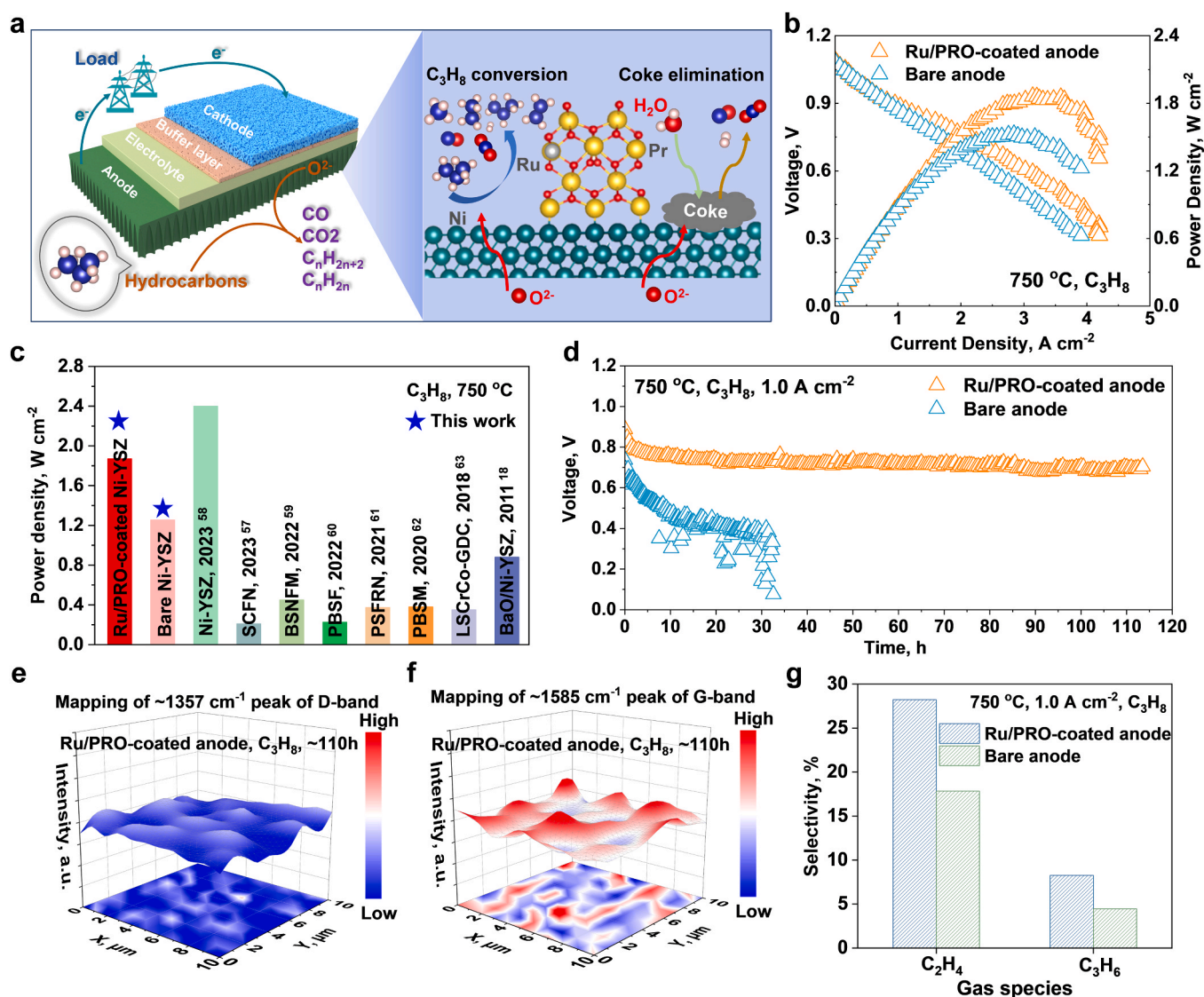


Fig. 4. Analyses of electrochemical performance, coking tolerance, and gas products on propane. (a) Schematic illustration of the SOFCs with the Ru/PRO-coated anode and the detailed schematics of coke removal process; (b) Typical I - V - P curves of bare and Ru/PRO-modified cells at 750 °C with 3 % H_2O humidified C_3H_8 as the fuel and ambient air as the oxidant; (c) Comparison of the PPDs of the state-of-the-art oxygen ion conductor SOFCs with C_3H_8 as the fuel; (d) The short-term durability of bare and Ru/PRO-modified cells when fueled by 3 % H_2O humidified C_3H_8 ; Typical Raman mapping of (e) D-band ($\sim 1357 \text{ cm}^{-1}$) and (f) G-band ($\sim 1585 \text{ cm}^{-1}$) for Ru/PRO-coated anode after the durability evaluation on C_3H_8 at 750 °C; (g) C_2H_4 and C_3H_6 selectivities over bare and Ru/PRO-coated anodes with a constant current density of 1.0 A cm^{-2} at 750 °C.

anode may react with the coke to form H_2 , CO , and CO_2 . The Ru/PRO catalyst could likely accelerate the coke elimination reactions and hence improve the coking tolerance of the anode, as confirmed by the durability test and Raman mapping.

Displayed in Fig. 4b are the I - V - P curves of bare and Ru/PRO-modified cells at $750^\circ C$ with 3 % H_2O humidified C_3H_8 as the fuel. A high peak power density of 1.870 W cm^{-2} was obtained in a Ru/PRO-modified cell, which is much higher than that in cells with the bare anode (1.530 W cm^{-2}), the Pr_6O_{11} -coated anode (1.682 W cm^{-2}), and the RuO_2 -coated anode (1.626 W cm^{-2}) (Figure S15, Supplementary Note 13). The corresponding EIS are displayed in Figure S16 (Supplementary Note 10). Shown in Fig. 4c is the comparison of the peak power densities of cells run on C_3H_8 at $750^\circ C$ [18,57–63]. Our cells with the Ru/PRO-coated anode demonstrated outstanding performance, only slightly lower than the ultra-high performance of $\sim 2.4\text{ W cm}^{-2}$ reported by Fang et al. recently [58]. Fig. 4d exhibits the short-term durability of bare and Ru/PRO-modified cells when fueled by 3 % H_2O humidified C_3H_8 at a constant current density of 1.0 A cm^{-2} and $750^\circ C$. The cell with the Ru/PRO-coated anode can be stably operated for $\sim 115\text{ h}$, indicating an excellent coking tolerance of the Ru/PRO-coated anode on propane (Figure S17, Supplementary Note 7). It is worth noting that the cells tend to exhibit rapid decay within the initial $\sim 10\text{ h}$, which may be attributed to the hydration process [24]. The anodes need sufficient water to assist the carbon removal process in this configuration. Concretely, water produced by the hydrogen oxidation reactions ($H_2 + 1/2 O_2 \rightarrow H_2O$) can be absorbed by the anode and used to remove the deposited carbon. As shown in Figure S18 (Supplementary Note 14), sharp carbon peaks (including D-band at $\sim 1357\text{ cm}^{-1}$ and G-band at $\sim 1585\text{ cm}^{-1}$) were observed in the Raman spectrum for a bare anode after being evaluated in C_3H_8 for $\sim 30\text{ h}$, while only weak carbon peaks were observed in the spectrum for the Ru/PRO-coated anode after being evaluated in C_3H_8 for $\sim 115\text{ h}$. A Raman mapping of the D-band and G-band peaks of the area of $10 \times 10\text{ }\mu\text{m}^2$ manifests that the coking that occurred on the Ru/PRO-coated anode surface is much less than that on the bare anode (Figs. 4e, 4f, and Figure S19) [24].

The off-gas composition becomes complex when C_3H_8 is fueled into the anode, mainly including H_2 , CO , CO_2 , CH_4 , C_2H_6 , C_2H_4 , C_3H_8 , and C_3H_6 (Figure S20, Supplementary Note 12). As shown in Fig. 4g, the C_2H_4 selectivity of the Ru/PRO-coated anode reaches 28.23 %, while the C_3H_6 selectivity reaches 8.26 %, both higher than that in the bare anode (17.83 % and 4.46 %). The off-gas in bare and Ru/PRO-coated anodes can only contain a small number of C_3H_8 in the gas products, indicating a high decomposition rate of C_3H_8 in the operation condition (Figure S21, Supplementary Note 12). The off-gas composition distribution of Pr_6O_{11} and RuO_2 -coated anodes is displayed in Figure S22 (Supplementary Note 12). Both Pr_6O_{11} and RuO_2 -coated anodes demonstrated increased C_2H_4 and C_3H_6 selectivities compared to the bare anode (Table. S3), indicating the synergistic catalytic effects of PrO_x and Ru. The results show the excellent potential of direct hydrocarbons SOFCs as the reactors for the co-generation of power and light olefins. Accordingly, this facile and highly scalable fabrication method could be widely applied to green and sustainable energy applications and petrochemical industries.

4. Conclusion

In summary, modifying the Ni-cermet anodes with Ru/PRO metal/oxide nano-heterostructured catalyst greatly enhanced the performance of direct hydrocarbons fuel cells, achieving the peak power densities of 1.784 and 1.870 W cm^{-2} on 3 % H_2O humidified CH_4 and C_3H_8 at $750^\circ C$, respectively. Moreover, cells with the Ru/PRO-coated anode can be stably operated on CH_4 for $\sim 220\text{ h}$ and C_3H_8 for $\sim 115\text{ h}$. The remarkable performance and coking tolerance of the anode are attributed to the efficient catalytic activity of the electrochemical oxidative hydrocarbon decomposition process and carbon removal process, as confirmed by the experiments and computations. Accordingly, the nano-

heterostructured Ru/PRO catalyst effectively boosts the coking tolerance and the kinetics of hydrocarbon decomposition. In addition to being attractive for direct hydrocarbon SOFCs, this design philosophy of restricted anode is also highly attractive for other types of energy conversion and storage systems, including membrane reactors for the synthesis of high-value-added chemicals.

CRediT authorship contribution statement

Yangsen Xu: Investigation, Data curation. **YongMan Choi:** Writing – review & editing, Supervision, Software, Resources, Methodology, Funding acquisition. **Kotaro Sasaki:** Software, Resources. **Fan He:** Investigation, Formal analysis. **Feng Zhu:** Investigation, Formal analysis. **Yu Chen:** Writing – review & editing, Supervision, Resources, Project administration, Methodology, Funding acquisition, Conceptualization. **Hua Zhang:** Investigation, Data curation. **Kang Xu:** Writing – original draft, Visualization, Validation, Investigation, Formal analysis, Data curation.

Declaration of Competing Interest

The authors declare that they have no known competing financial interests or personal relationships that could have appeared to influence the work reported in this paper.

Data Availability

Data will be made available on request.

Acknowledgments

This study was supported by the Guangdong Innovative and Entrepreneurial Research Team Program (2021ZT09L392), the Pearl River Talent Recruitment Program (2019QN01C693), the National Natural Science Foundation of China (22179039), the Fundamental Research Funds for the Central Universities (2022ZYGXZR002), Guangdong Basic and Applied Basic Research Foundation), and Zijin Mining Group Co., Ltd (5405-ZC-2023-00008). Computational studies were supported by the National Science and Technology Council (NSTC Grant No. 110-2221-E-A49-017-MY3 and 111-2221-E-A49-003-MY3), the National Center for High-performance Computing (NCHC), and the Higher Education Sprout Project of the National Yang Ming Chiao Tung University and Ministry of Education (MOE), Taiwan. DFT calculations were performed using the resources of the Center for Functional Nanomaterials, which is a U.S. DOE Office of Science Facility, at Brookhaven National Laboratory under Contract No. DE-SC0012704.

Methods

The details of powder synthesis, catalyst preparation, cell fabrication, materials and microstructure characterization, electrochemical measurements, and computational details are provided in Supplementary Information.

Appendix A. Supporting information

Supplementary data associated with this article can be found in the online version at [doi:10.1016/j.apcatb.2024.124208](https://doi.org/10.1016/j.apcatb.2024.124208).

References

- [1] C. Duan, R.J. Kee, H. Zhu, C. Karakaya, Y. Chen, S. Ricote, A. Jarry, E.J. Crumlin, D. Hook, R. Braun, N.P. Sullivan, R. O'Hayre, Highly durable, coking and sulfur tolerant, fuel-flexible protonic ceramic fuel cells, *Nature* 557 (2018) 217–222.
- [2] T.H. Shin, S. Ida, T. Ishihara, Doped CeO_2 - $LaFeO_3$ composite oxide as an active anode for direct hydrocarbon-type solid oxide fuel cells, *J. Am. Chem. Soc.* 133 (2011) 19399–19407.

- [3] Y. Chen, B. deGlee, Y. Tang, Z. Wang, B. Zhao, Y. Wei, L. Zhang, S. Yoo, K. Pei, J. H. Kim, Y. Ding, P. Hu, F.F. Tao, M. Liu, A robust fuel cell operated on nearly dry methane at 500 °C enabled by synergistic thermal catalysis and electrocatalysis, *Nat. Energy* 3 (2018) 1042–1050.
- [4] Z. Zhan, A. Barnett Scott, An octane-fueled solid oxide fuel cell, *Science* 308 (2005) 844–847.
- [5] S. Park, J.M. Vohs, R.J. Gorte, Direct oxidation of hydrocarbons in a solid-oxide fuel cell, *Nature* 404 (2000) 265–267.
- [6] T. Gan, H. Song, X. Fan, Y. Liu, S. Liu, Y. Zhao, Y. Li, A rational design of highly active and coke-resistant anode for methanol-fueled solid oxide fuel cells with Sn doped Ni-Ce_{0.8}Sm_{0.2}O_{2-δ}, *Chem. Eng. J.* 455 (2023) 140692.
- [7] P.I. Cowin, C.T.G. Petit, R. Lan, J.T.S. Irvine, S. Tao, Recent progress in the development of anode materials for solid oxide fuel cells, *Adv. Energy Mater.* 1 (2011) 314–332.
- [8] C. Zhu, S. Hou, X. Hu, J. Lu, F. Chen, K. Xie, Electrochemical conversion of methane to ethylene in a solid oxide electrolyzer, *Nat. Commun.* 10 (2019) 1173.
- [9] I. Alstrup, A new model explaining carbon filament growth on nickel, iron, and Ni Cu alloy catalysts, *J. Catal.* 109 (1988) 241–251.
- [10] Z. Ma, C. Sun, C. Ma, H. Wu, Z. Zhan, L. Chen, Ni doped La_{0.6}Sr_{0.4}FeO_{3-δ} symmetrical electrode for solid oxide fuel cells, *Chin. J. Catal.* 37 (2016) 1347–1353.
- [11] S. Tao, J.T.S. Irvine, A redox-stable efficient anode for solid-oxide fuel cells, *Nat. Mater.* 2 (2003) 320–323.
- [12] Y.-H. Huang, R.I. Dass, Z.-L. Xing, J.B. Goodenough, Double perovskites as anode materials for solid-oxide fuel cells, *Science* 312 (2006) 254–257.
- [13] J.C. Ruiz-Morales, J. Canales-Vázquez, C. Savaniu, D. Marrero-López, W. Zhou, J.T. S. Irvine, Disruption of extended defects in solid oxide fuel cell anodes for methane oxidation, *Nature* 439 (2006) 568–571.
- [14] N. Hou, T. Yao, P. Li, X. Yao, T. Gan, L. Fan, J. Wang, X. Zhi, Y. Zhao, Y. Li, A-site ordered double perovskite with in situ exsolved core-shell nanoparticles as anode for solid oxide fuel cells, *ACS Appl. Mater. Interfaces* 11 (2019) 6995–7005.
- [15] T. Tan, Z. Wang, K. Huang, C. Yang, High-performance co-production of electricity and light olefins enabled by exsolved NiFe alloy nanoparticles from a double-perovskite oxide anode in solid oxide-ion-conducting fuel cells, *ACS Nano* 17 (2023) 13985–13996.
- [16] Y. Zhang, B. Chen, D. Guan, M. Xu, R. Ran, M. Ni, W. Zhou, R. O'Hayre, Z. Shao, Thermal-expansion offset for high-performance fuel cell cathodes, *Nature* 591 (2021) 246–251.
- [17] M. Li, B. Hua, J.-I. Luo, S.P. Jiang, J. Pu, B. Chi, L. Jian, Carbon-tolerant Ni-based cermet anodes modified by proton conducting yttrium- and ytterbium-doped barium cerates for direct methane solid oxide fuel cells, *J. Mater. Chem. A* 3 (2015) 21609–21617.
- [18] L. Yang, Y. Choi, W. Qin, H. Chen, K. Blinn, M. Liu, P. Liu, J. Bai, T.A. Tyson, M. Liu, Promotion of water-mediated carbon removal by nanostructured barium oxide/nickel interfaces in solid oxide fuel cells, *Nat. Commun.* 2 (2011) 357.
- [19] T. Hu, F. He, M. Liu, Y. Chen, In situ/operando regulation of the reaction activities on hetero-structured electrodes for solid oxide cells, *Prog. Mater. Sci.* 133 (2023) 101050.
- [20] Y. Zhu, S. Zhang, Y. Ye, X. Zhang, L. Wang, W. Zhu, F. Cheng, F. Tao, Catalytic conversion of carbon dioxide to methane on ruthenium-cobalt bimetallic nanocatalysts and correlation between surface chemistry of catalysts under reaction conditions and catalytic performances, *ACS Catal.* 2 (2012) 2403–2408.
- [21] Z. Xiao, X. Zhang, L. Wang, G. Li, Optimizing the preparation of Ni-Ce-Pr catalysts for efficient hydrogen production by n-dodecane steam reforming, *Int. J. Energy Res.* 44 (2020) 1828–1842.
- [22] A. Salcedo, I. Iglesias, F. Mariño, B. Irigoyen, Promoted methane activation on doped ceria via occupation of Pr(4f) states, *Appl. Surf. Sci.* 458 (2018) 397–404.
- [23] O. Bezkravnyi, M. Vorokhta, M. Pawlyta, M. Ptak, L. Pilai, X. Xie, T.N. Dinhová, I. Khalakhan, I. Matolínová, L. Kepinski, In situ observation of highly oxidized Ru species in Ru/CeO₂ catalyst under propane oxidation, *J. Mater. Chem. A* 10 (2022) 16675–16684.
- [24] K. Xu, H. Zhang, W. Deng, Y. Liu, Y. Ding, Y. Zhou, M. Liu, Y. Chen, Self-hydrating of a ceria-based catalyst enables efficient operation of solid oxide fuel cells on liquid fuels, *Sci. Bull.* 68 (2023) 2574–2582.
- [25] F. Liu, H. Deng, H. Ding, P. Kazempoor, B. Liu, C. Duan, Process-intensified protonic ceramic fuel cells for power generation, chemical production, and greenhouse gas mitigation, *Joule* 7 (2023) 1308–1332.
- [26] Y. Zhang, J. Deng, H. Zhang, Y. Liu, H. Dai, Three-dimensionally ordered macroporous Pr₆O₁₁ and Tb₄O₇ with mesoporous walls: Preparation, characterization, and catalytic activity for CO oxidation, *Catal. Today* 245 (2015) 28–36.
- [27] J. Lu, Y. Lei, G. Wan, Z. Mei, J. Yu, Y. Zhao, S. He, Y. Luo, Weakening the metal-support strong interaction to enhance catalytic performances of alumina supported Ni-based catalysts for producing hydrogen, *Appl. Catal., B* 263 (2020) 118177.
- [28] B.-K. Park, R. Scipioni, D. Cox, S.A. Barnett, Enhancement of Ni-(Y₂O₃)_{0.08}(ZrO₂)_{0.92} fuel electrode performance by infiltration of Ce_{0.8}Gd_{0.2}O_{2-δ} nanoparticles, *J. Mater. Chem. A* 8 (2020) 4099–4106.
- [29] J.G. Rix, B. Mo, A.Y. Nikiforov, U.B. Pal, S. Gopalan, S.N. Basu, Quantifying percolated triple phase boundary density and its effects on anodic polarization in Ni-infiltrated Ni/YSZ SOFC anodes, *J. Electrochem. Soc.* 168 (2021) 114507.
- [30] K. Xu, H. Zhang, Y. Xu, F. He, Y. Zhou, Y. Pan, J. Ma, B. Zhao, W. Yuan, Y. Chen, M. Liu, An efficient steam-induced heterostructured air electrode for protonic ceramic electrochemical cells, *Adv. Funct. Mater.* 32 (2022) 2110998.
- [31] Y. Sha, Y. Ling, Y. Yang, X. Wang, D. Meng, S. Wang, A finger-like anode with infiltrated Ni_{0.1}Ce_{0.9}O_{2-δ} catalyst using new phase inversion combined tape-casting technology for optimized dry reforming of methane, *Ceram. Int.* 49 (2023) 29155–29163.
- [32] T. Yang, S.L. Kollasch, J. Grimes, A. Xue, S.A. Barnett, La_{0.8}Sr_{0.2}O_{0.98}MnO_{3-δ} Zr_{0.92}Y_{0.16}O_{2-δ}PrO_x for oxygen electrode supported solid oxide cells, *Appl. Catal., B* 306 (2022) 121114.
- [33] Y. Lim, J. Park, H. Lee, M. Ku, Y.-B. Kim, Rapid fabrication of lanthanum strontium cobalt ferrite (LSCF) with suppression of LSCF/YSZ chemical side reaction via flash light sintering for SOFCs, *Nano Energy* 90 (2021) 106524.
- [34] Y.-D. Kim, J.-Y. Yang, M. Saqib, K. Park, J.-S. Shin, M. Jo, K.M. Park, H.-T. Lim, S.-J. Song, J.-Y. Park, Cobalt-free perovskite Ba_{1-x}Nd_xFeO_{3-δ} air electrode materials for reversible solid oxide cells, *Ceram. Int.* 47 (2021) 7985–7993.
- [35] K. Xu, K. Pei, B. Zhao, Y. Zhao, Q. Niu, Y. Chen, An oxygen reduction reaction active and durable SOFC cathode/electrolyte interface achieved via a cost-effective spray-coating, *Int. J. Hydrog. Energy* 46 (2021) 32242–32249.
- [36] N. Duan, J. Yang, M. Gao, B. Zhang, J.-L. Luo, Y. Du, M. Xu, L. Jia, B. Chi, J. Li, Multi-functionalities enabled fivefold applications of LaCo_{0.6}Ni_{0.4}O_{3-δ} in intermediate temperature symmetrical solid oxide fuel/electrolysis cells, *Nano Energy* 77 (2020) 105207.
- [37] Z. Lyu, Y. Wang, Y. Zhang, M. Han, Solid oxide fuel cells fueled by simulated biogas: comparison of anode modification by infiltration and reforming catalytic layer, *Chem. Eng. J.* 393 (2020) 124755.
- [38] S.-L. Zhang, H. Wang, T. Yang, M.Y. Lu, C.-X. Li, C.-J. Li, S.A. Barnett, Advanced oxygen-electrode-supported solid oxide electrochemical cells with Sr(Ti,Fe)O_{3-δ}-based fuel electrodes for electricity generation and hydrogen production, *J. Mater. Chem. A* 8 (2020) 25867–25879.
- [39] J. Kim, J. Ahn, J. Shin, K.J. Yoon, J.-W. Son, J.-H. Lee, D. Shin, H.-W. Lee, H.-I. Ji, Enhanced sinterability and electrochemical performance of solid oxide fuel cells via a roll calendaring process, *J. Mater. Chem. A* 7 (2019) 9958–9967.
- [40] S. Li, L. Zhang, T. Xia, Q. Li, L. Sun, L. Huo, H. Zhao, Synergistic effect study of EuBa_{0.98}Co₂O_{5+δ}-Ce_{0.8}Sm_{0.2}O_{1.9} composite cathodes for intermediate-temperature solid oxide fuel cells, *J. Alloy. Compd.* 771 (2019) 513–521.
- [41] Z. Zhu, M. Li, C. Xia, H.J.M. Bouwmeester, Bismuth-doped La_{1.75}Sr_{0.25}NiO_{4+δ} as a novel cathode material for solid oxide fuel cells, *J. Mater. Chem. A* 5 (2017) 14012–14019.
- [42] N. Ai, N. Li, S. He, Y. Cheng, M. Saunders, K. Chen, T. Zhang, S.P. Jiang, Highly active and stable Er_{0.4}Bi_{1.6}O₃ decorated La_{0.76}Sr_{0.19}MnO_{3+δ} nanostructured oxygen electrodes for reversible solid oxide cells, *J. Mater. Chem. A* 5 (2017) 12149–12157.
- [43] Y. Jeon, J.-H. Myung, S.-H. Hyun, Y.-G. Shul, J.T.S. Irvine, Corn-cob like nanofibres as cathode catalysts for an effective microstructure design in solid oxide fuel cells, *J. Mater. Chem. A* 5 (2017) 3966–3973.
- [44] J.S.A. Carneiro, R.A. Brocca, M.L.R.S. Lucena, E. Nikolla, Optimizing cathode materials for intermediate-temperature solid oxide fuel cells (SOFCs): Oxygen reduction on nanostructured lanthanum nickelate oxides, *Appl. Catal., B* 200 (2017) 106–113.
- [45] M. Li, K. Chen, B. Hua, J.-I. Luo, W.D.A. Rickard, J. Li, J.T.S. Irvine, S.P. Jiang, Smart utilization of cobaltite-based double perovskite cathodes on barrier-layer-free zirconia electrolyte of solid oxide fuel cells, *J. Mater. Chem. A* 4 (2016) 19019–19025.
- [46] K. Chen, N. Li, N. Ai, M. Li, Y. Cheng, W.D.A. Rickard, J. Li, S.P. Jiang, Direct application of cobaltite-based perovskite cathodes on the yttria-stabilized zirconia electrolyte for intermediate temperature solid oxide fuel cells, *J. Mater. Chem. A* 4 (2016) 17678–17685.
- [47] L. Lu, C. Ni, M. Cassidy, J.T.S. Irvine, Demonstration of high performance in a perovskite oxide supported solid oxide fuel cell based on La and Ca co-doped SrTiO₃, *J. Mater. Chem. A* 4 (2016) 11708–11718.
- [48] S. Sengodan, S. Choi, A. Jun, T.H. Shin, Y.-W. Ju, H.Y. Jeong, J. Shin, J.T.S. Irvine, G. Kim, Layered oxygen-deficient double perovskite as an efficient and stable anode for direct hydrocarbon solid oxide fuel cells, *Nat. Mater.* 14 (2015) 205–209.
- [49] D. Chen, Y. Huan, G. Ma, M. Ma, X. Wang, X. Xie, J. Leng, X. Hu, T. Wei, High-entropy alloys FeCoNiCuX (X = Al, Mo)-Ce_{0.8}Sm_{0.2}O₂ as high-performance solid oxide fuel cell anodes, *ACS Appl. Energy Mater.* 6 (2023) 1076–1084.
- [50] T. Wang, R. Wang, X. Xie, S. Chang, T. Wei, D. Dong, Z. Wang, Robust direct hydrocarbon solid oxide fuel cells with exsolved anode nanocatalysts, *ACS Appl. Mater. Interfaces* 14 (2022) 56735–56742.
- [51] Y. Tang, H. Wang, R. Wang, Q. Liu, Z. Yan, L. Xu, X. Liu, Synergistically promoting coking resistance of a La_{0.4}Sr_{0.4}Ti_{0.85}Ni_{0.15}O_{3-δ} anode by Ru-doping-induced active twin defects and highly dispersed Ni nanoparticles, *ACS Appl. Mater. Interfaces* 14 (2022) 44002–44014.
- [52] Y. Liu, L. Jia, J. Li, B. Chi, J. Pu, J. Li, High-performance Ni in-situ exsolved Ba (Ce_{0.9}Y_{0.1})_{0.8}Ni_{0.2}O_{3-δ}/Gd_{0.1}Ce_{0.9}O_{1.95} composite anode for SOFC with long-term stability in methane fuel, *Compos. Part B* 193 (2020) 108033.
- [53] H. Chang, H. Chen, G. Yang, W. Zhou, J. Bai, S. Li, Z. Shao, Enhanced coking resistance of a Ni cermet anode by a chromates protective layer, *J. Energy Chem.* 37 (2019) 117–125.
- [54] L. Bian, C. Duan, L. Wang, R. O'Hayre, J. Cheng, K.-C. Chou, Ce-doped La_{0.7}Sr_{0.3}Fe_{0.9}Ni_{0.1}O_{3-δ} as symmetrical electrodes for high performance direct hydrocarbon solid oxide fuel cells, *J. Mater. Chem. A* 5 (2017) 15253–15259.
- [55] A. Salcedo, P.G. Lustemberg, N. Rui, R.M. Palomino, Z. Liu, S. Nemsak, S. D. Senanayake, J.A. Rodriguez, M.V. Ganduglia-Pirovano, B. Irigoyen, Reaction pathway for coke-free methane steam reforming on a Ni/CeO₂ Catalyst: active sites and the role of metal-support interactions, *ACS Catal.* 11 (2021) 8327–8337.
- [56] M. Shishkin, T. Ziegler, Oxidation of H₂, CH₄, and CO molecules at the interface between Nickel and Yttria-Stabilized Zirconia: a theoretical study based on DFT, *J. Phys. Chem. C* 113 (2009) 21667–21678.

- [57] C. Shi, Y. Liu, B. Wang, B. Niu, C. Lu, Nb-doped double perovskite $\text{Sr}_2\text{CoFeO}_{6-\delta}$ as an efficient and prospective electrode for quasi-symmetrical solid oxide fuel cells, *Mater. Lett.* 350 (2023) 134892.
- [58] L. Fang, F. Liu, D. Diercks, P. Kumar, F. Zhao, D. Ding, C. Duan, Boosting the performance of reversible solid oxide electrochemical cells with a novel hybrid oxygen electrode, $\text{Pr}_{1.39}\text{Ba}_{0.14}\text{Sr}_{0.53}\text{Co}_{1.48}\text{Fe}_{0.76}\text{O}_{6-\delta}\text{-Ba}_{0.66}\text{Sr}_{0.34}\text{CoO}_{3-\delta}$, *J. Mater. Chem. A* 11 (2023) 21251–21262.
- [59] H. Yang, M. La, Z. Wang, T. Tan, M. Qin, J. Hu, C. Yang, In situ exsolved $\text{NiFe}/(\text{NiFe})\text{O}_x$ core-shell-structured nanocatalysts on perovskite anode with enhanced coking resistance, *ACS Sustain. Chem. Eng.* 10 (2022) 12510–12519.
- [60] C. Wen, K. Chen, D. Guo, W. Yang, S. Gao, C. Lu, B. Niu, B. Wang, High performance and stability of $\text{PrBa}_{0.5}\text{Sr}_{0.5}\text{Fe}_2\text{O}_{5+\delta}$ symmetrical electrode for intermediate temperature solid oxide fuel cells, *Solid State Ion.* 386 (2022) 116048.
- [61] M. Qin, Y. Xiao, H. Yang, T. Tan, Z. Wang, X. Fan, C. Yang, Ru/Nb co-doped perovskite anode: achieving good coking resistance in hydrocarbon fuels via core-shell nanocatalysts exsolution, *Appl. Catal., B* 299 (2021) 120613.
- [62] S. Choi, Electrochemical properties of Sr-doped layered perovskite as a promising anode material for direct hydrocarbon SOFCs, *J. Korean Ceram. Soc.* 57 (2020) 409–415.
- [63] K.-Y. Lai, A. Manthiram, Self-regenerating Co–Fe nanoparticles on perovskite oxides as a hydrocarbon fuel oxidation catalyst in solid oxide fuel cells, *Chem. Mater.* 30 (2018) 2515–2525.